

ADVANCED MATERIALS

Supporting Information

for *Adv. Mater.*, DOI: 10.1002/adma.201908176

Infrared Permittivity of the Biaxial van der Waals
Semiconductor #-MoO₃ from Near- and Far-Field Correlative
Studies

*Gonzalo Álvarez-Pérez, Thomas G. Folland, Ion Errea, Javier
Taboada-Gutiérrez, Jiahua Duan, Javier Martín-Sánchez, Ana
I. F. Tresguerres-Mata, Joseph R. Matson, Andrei Bylinkin,
Mingze He, Weiliang Ma, Qiaoliang Bao, José Ignacio
Martín,
Joshua D. Caldwell,* Alexey Y. Nikitin,* and Pablo Alonso-
González**

Supporting Information

Infrared Permittivity of the Biaxial van der Waals Semiconductor α -MoO₃ from Near- and Far-Field Correlative Studies

Gonzalo Álvarez-Pérez, Thomas G. Folland, Ion Errea, Javier Taboada-Gutiérrez, Jiahua Duan, Javier Martín-Sánchez, Ana I. F. Tresguerres-Mata, Joseph R. Matson, Andrei Bylinkin, Mingze He, Weiliang Ma, Qiaoliang Bao, José Ignacio Martín, Joshua D. Caldwell, Alexey Y. Nikitin* and Pablo Alonso-González.**

Contents

- S1. AgCl dielectric function
- S2. Polarized FTIR transmission spectra
- S3. Fit sensitivity of α -MoO₃ far-field data
- S4. Thickness and geometry of α -MoO₃ flakes
- S5. IR dielectric function of α -MoO₃, from far-field measurements
- S6. BaF₂ dielectric function
- S7. Propagation lengths and wavelengths of PhPs in α -MoO₃ from experimental s-SNOM profiles and full-wave numerical simulations
- S8. Attenuated total reflectance spectra (ATR) of an α -MoO₃ flake on top of BaF₂
- S9. Comparison of our IR dielectric function parameters with prior experimental results
- S10. Permittivity of α -MoO₃ from first principles
- S11. THz/far-IR transmission spectra collected from α -MoO₃ powder using a Nb-superconducting bolometer

References

S1. AgCl dielectric function

The infrared dielectric function of AgCl was extracted using the methods described in the main text. In brief, a 2-mm-thick AgCl window is mounted in the bench of a Fourier transform infrared (FTIR) spectrometer, and unpolarized reflection and transmission data are taken using a room temperature pyroelectric DLaTGs detector into the far infrared (**Figure S1a**). These data are fit using JA Wollams VASE software, using a phenomenological model with multiple Gaussian oscillators of the functional form

$$\varepsilon(E) = \varepsilon_{\infty} + \sum_{n=1}^3 \varepsilon_1^n + i\varepsilon_2^n, \quad (\text{S1})$$

$$\varepsilon_2^n(E) = A_n e^{-\left(\frac{E-E_n}{\sigma_n}\right)^2} - A_n e^{-\left(\frac{E+E_n}{\sigma_n}\right)^2},$$

$$\varepsilon_1^n(E) = \frac{2}{\pi} P \int_0^{\infty} \frac{\xi \varepsilon_2^n(\xi)}{\xi^2 - E^2} d\xi,$$

$$\sigma = \frac{Br_n}{2\sqrt{\ln(2)}},$$

where A_n is the amplitude, Br_n is the full width at half maximum (FWHM) of the gaussian, E is the frequency, E_n is the center frequency and P is the Cauchy principal value. This model has been deliberately over-parameterized, and whilst it provides a good dielectric function fit, it does not provide physical information (such as phonon energies) about AgCl itself. The tabulated values for the fit are shown in **Table S1**. The dielectric function associated with this material is shown in Figure S1b, showing minimal dispersion in the region of interest for our experiments on α -MoO₃ samples.

$\varepsilon_{\infty} = 4.89$	A_n	E_n	Br_n
Oscillator 1	1.14	12.3	266
Oscillator 2	11.5	94.7	30.1
Oscillator 3	69.0	13.3	153

Table S1. Fitting parameters for our AgCl dielectric function model.

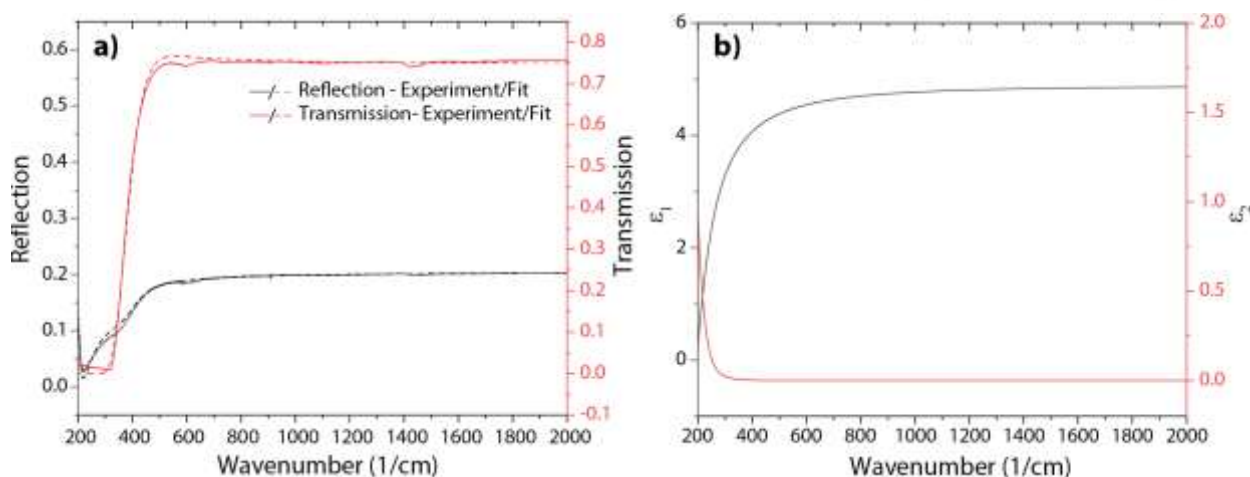


Figure S1. IR optical response (a) and fitted dielectric function (b) of AgCl.

S2. Polarized FTIR transmission spectra.

Transmission spectra were also taken through our sample of α -MoO₃, as shown in **Figure S2**.

Whilst the spectral features of the transmission spectra are generally well reproduced, we note that the amplitudes of the transmission spectra are significantly offset. This is largely due to the collection of infrared light which is not transmitted through the crystal and prevents the use of these spectra for fitting. We also observe broad absorption bands between 1050 and 1150 cm⁻¹ which are not accounted for in our model. These are likely associated with weak multi-phonon processes in the α -MoO₃ flake.

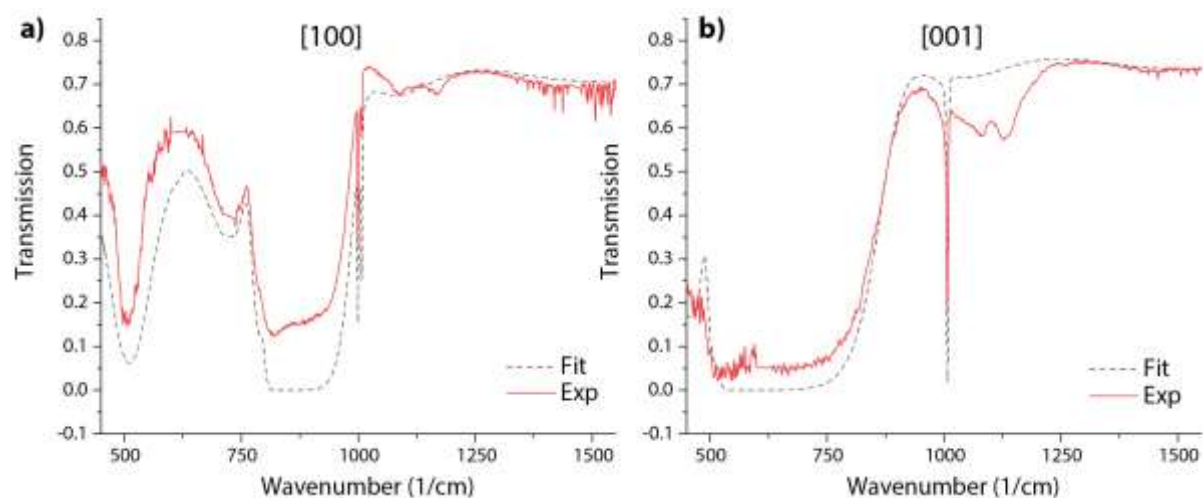


Figure S2. Transmission spectra along [100] or x axis (a), and along [001] or y axis (b).

S3. Fit sensitivity of α -MoO₃ far-field data.

In this section we will assess fit ‘uniqueness’, to demonstrate the limitations of the far-field model—notably the limitations when it comes to phonon damping. A completely ‘unique’ parameter can be fit without coupling to any other parameters in the model, i.e. its value will be determined by some unique feature in the spectrum (for example a peak frequency). Fit uniqueness studies were performed by fixing the parameter under study at several values close to the global minimum, and then fitting all other parameters. We can then examine how much the mean squared error (MSE) increases relative to the global minimum value. Rapid increases in the MSE to small variations in the parameter value indicate a ‘unique’ and well fitted parameter, and vice versa. In this case we choose to analyze the parameters associated with the primary RB in the x direction: ω_{TO} , ω_{LO} , γ and ϵ_{∞} (results shown in **Figure S3**).

The TO phonon clearly possesses the most unique fit value, with extremely strong increase in MSE away from the fitted frequency. The LO phonon, epsilon infinity and damping values show less dramatic variations in the MSE when compared to their global minimum value. In order to quantitatively compare all 4 parameters that fit our studies, we can use a figure of merit. We define the FOM as the change in the fit parameter when the MSE is increased by 1% of the global minimum, divided by the value at the global minimum. For the TO phonon we get 0.4%, for the LO phonon we get 0.6%, for epsilon infinity we get 4%, and for damping 96%. This demonstrates how our far-field fit is extremely weakly sensitive to the phonon damping value. We also note that the epsilon infinity value is not as unique as the TO and LO phonon energies. This is because non-idealities introduced into the model (nominally the amount of reflection collected, as well as the precise thickness) have coupling for this parameter.

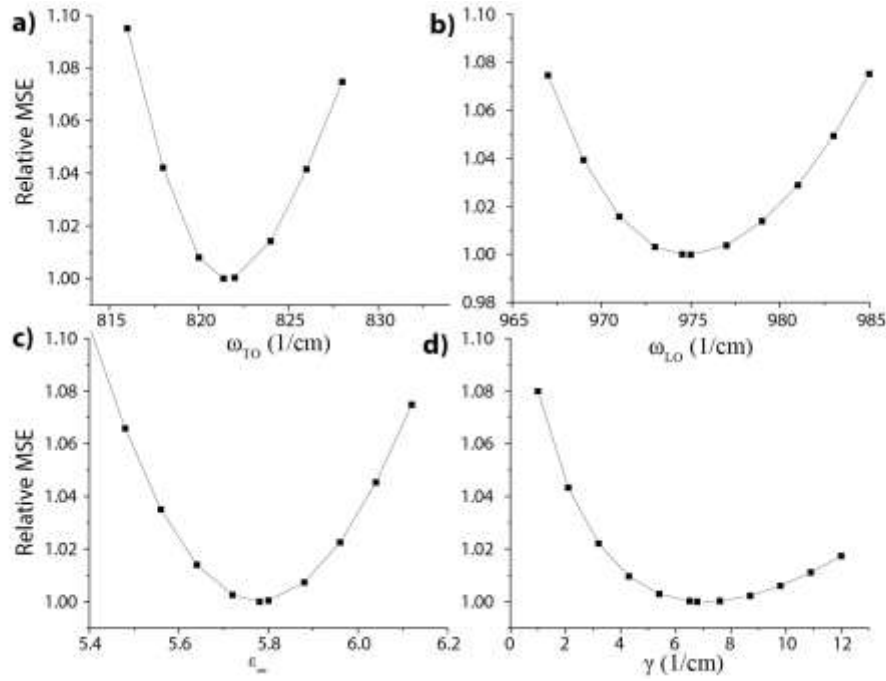


Figure S3. Fit uniqueness for the (a) TO phonon energy (b) LO phonon energy (c) epsilon infinity and (d) damping for the strong phonon band in [100] or x direction.

While the fit uniqueness value suggests that TO and LO energy values should be accurately determined from far-field data, coupling between parameters can complicate matters. Here we consider the coupling between the epsilon infinity value (which has dependence on experimental non-idealities) and the TO and LO phonon energies (**Figure S4**). We see that the epsilon infinity value couples to the LO phonon energy. This means that any error in the determination in epsilon infinity introduced by the experimental non-idealities and any associated local minima will have a knock-on effect on the LO phonon energy. Most notably, any inaccuracy in the thickness of the flake, as well as the percentage of the 1st reflection collected, can influence the value of epsilon infinity. The data from s-SNOM allows us to jump out of local minima, and find the best, and most realistic fit parameters.

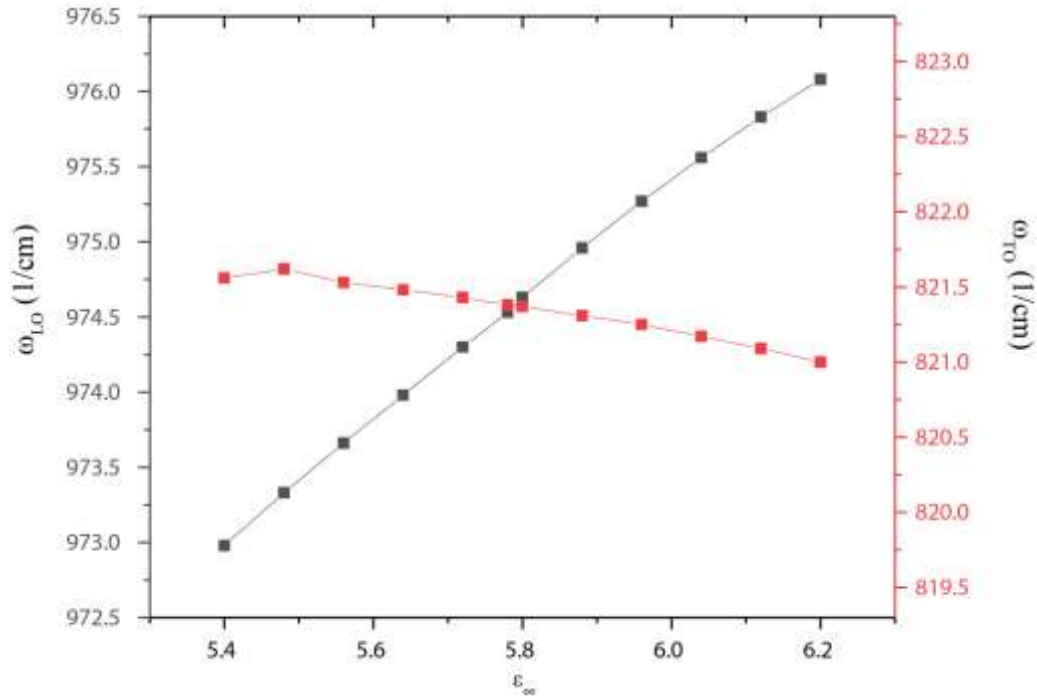


Figure S4. Coupling between epsilon infinity and LO phonon values.

S4. Thickness and geometry of α -MoO₃ flakes

To extract material parameters with high accuracy, the geometry of the sample can be critical. In particular, the thickness of the flake has great influence both on the fitting of the FTIR spectra and in the PhP wavelength. The thicknesses of the α -MoO₃ flakes used throughout this work were determined using standard methods. On the one hand, the thickness of the flake employed in our far-field FTIR characterization was measured with a contact profilometer, while that of the thinner flake, used in near-field s-SNOM imaging, was determined via atomic force microscopy (AFM).

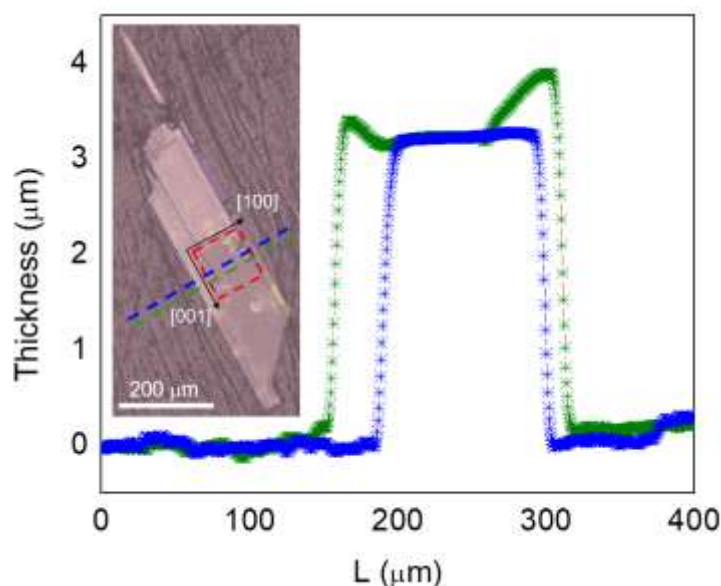


Figure S5. Determination of the thickness of the α -MoO₃ flake used for FTIR spectroscopy. The measurement was done using a contact profilometer, along the lines depicted in blue and green in the inset. The red square shows the area in which the FTIR spectra were acquired.

The thickness of the α -MoO₃ flake in which the FTIR spectra were acquired was determined using a contact profilometer (**Figure S5**), yielding a value of 3 ± 0.2 μm . Even though profilometers can be very accurate, we have considered an error of 200 nm bearing in mind i) the pressure exerted by the stylus onto the AgCl substrate, which is very soft, and ii) that the thickness is not perfectly constant in the area in which the FTIR spectra were acquired.

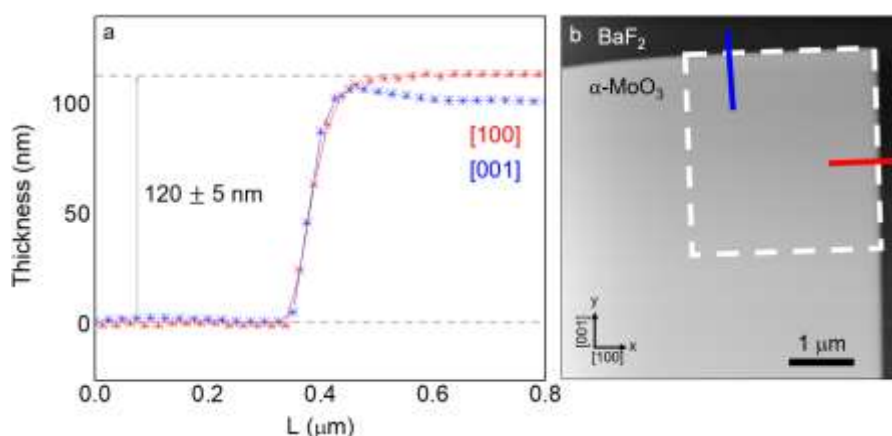


Figure S6. α -MoO₃ flake used for s-SNOM imaging. **a.** AFM profile along the two orthogonal in-plane directions: the flake thickness is 120 ± 5 nm. **b.** AFM image of the 90-degree-like corner used for near-field imaging, The white square shows the area in which s-SNOM imaging was performed.

Figure S6 shows an AFM image of the α -MoO₃ flake used for near-field imaging. Since the specific geometry of the edges of the flake can affect the near field distributions of PhPs, the corner in which we tested the predictive capabilities of our model was 90-degree-like. Averaging line profiles along both in plane directions, we obtain a flake thickness of 120 ± 5 nm, where the error stands for the thickness deviation along the flake edge and from data processing. Such profiles also show that the corners are steep and regular along the [010] or z direction, as needed for homogeneous launching of PhPs.

S5. IR dielectric function of α -MoO₃, from far-field measurements

Table S2. Parameters for the IR dielectric function of α -MoO₃, extracted from far-field experiments. The high-frequency permittivities are $\epsilon_x^\infty = 5.78$, $\epsilon_y^\infty = 6.07$ and $\epsilon_z^\infty = 4.47$ (fixed to the *ab-initio* value) for the experiment. The flake thickness used in the fit was 2.9 μ m.

Main axis	Mode index			
i	j	ω_{ij}^{T0} (cm ⁻¹)	ω_{ij}^{L0} (cm ⁻¹)	γ_{ij} (cm ⁻¹)
x	1	506.7	534.3	49.1
x	2	821.4	974.5	6.8
x	3	998.7	999.2	0.35
y	1	544.6	850.1	9.5
z	1	956.7	1006.9	0.65

S6. BaF₂ dielectric function

The infrared dielectric function of BaF₂ was extracted using analogous methods as the ones described in Section S1 for extracting the dielectric function of AgCl: using a phenomenological model with multiple Gaussian oscillators of the functional form in **Equation (S1)**. As that, this model for BaF₂ has been deliberately over-parameterized, and whilst it provides a good dielectric function fit, it does not provide physical information about BaF₂ itself. The tabulated values are provided in **Table S3**, while the infrared optical response and the fitted IR dielectric function of this material are shown in **Figure S5**, showing minimal dispersion in the region of interest for our experiments on α -MoO₃ samples.

$\varepsilon_\infty = 2.68$	A_n	E_n	B_n
Oscillator 1	1551.5	189.46	9.77
Oscillator 2	2389.9	17.69	388.91
Oscillator 3	0.1110	34.31	560.57

Table S3. Fitting parameters for our BaF₂ dielectric function model.

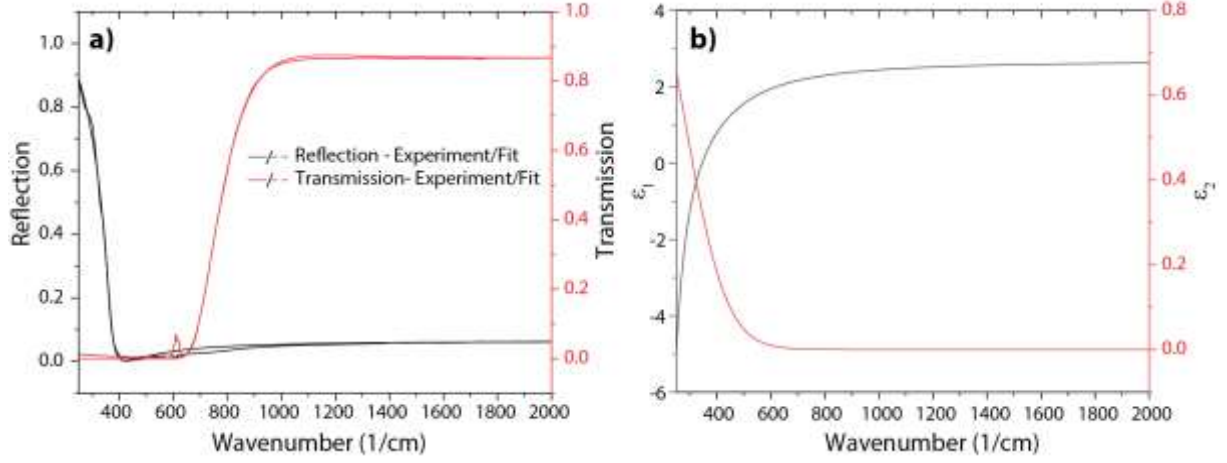


Figure S7. IR optical response (a) and fitted dielectric function (b) of BaF₂.

S7. Propagation lengths and wavelengths of PhPs in α -MoO₃ from experimental s-SNOM profiles and full-wave numerical simulations

The PhP propagation length L_p and wavelength λ_p is obtained by fitting line profiles of the polaritonic near field along the [100] and [001] crystal directions to oscillating signals with a factor accounting for dissipation described by an exponential decay of the PhPs field with distance x . The decay of polaritons away from an edge is due to a combination of damping ($\text{Im}(q_p) > 0$) and circular-wave geometrical spreading.^[1,2] Thus, the oscillating signal of the polaritonic near field can be fitted with

$$\xi_{opt}(x) = \xi_0 + A \frac{e^{i2kx}}{\sqrt{x}} + B \frac{e^{ikx}}{x^a}, \quad A, B, a > 0 \quad (\text{S2})$$

where k is the complex PhP wavevector. The first term is the returning (to the s-SNOM tip) field for a damped circular wave reflected from a straight edge, with the PhP travelling a distance $2x$. The second term interferes with the first, producing alternating fringe amplitudes. It arises because PhPs are not only generated/detected beneath the tip apex, but also at the edge of the flake travelling a distance x . **Equation S2** can be easily transformed into

$$\xi_{opt}(x) = \xi_0 + A \frac{e^{-\frac{2x}{L_p} \sin\left(4\pi \frac{x-A}{\lambda_p}\right)}}{\sqrt{x}} + B \frac{e^{-\frac{x}{L_p} \sin\left(2\pi \frac{x-B}{\lambda_p}\right)}}{x^a}, \quad A, B, L_p, \lambda_p, a > 0, \quad (\text{S3})$$

From the fitting procedure in **Equation (S3)** we directly extract the simulated and experimental PhP propagation length L_p and wavelength λ_p . To fit the simulated profiles, we fix $A = 0$ and $a = 1/2$, as PhPs in our full-wave numerical simulations are launched by a point dipole (therefore there are no edge-launched waves), and just λ_p -periodic waves with circular geometrical decay are present. On the other hand, in the experimental profiles, both contributions are present: in this case, since the geometrical decay of the PhP travelling the tip–edge distance only once is not known a priori, we allow for a variable decay^[1] $a \sim 1$. **Figure S8** shows the profiles and the fittings performed to extract the polaritonic wavelength and propagation length, as well as theoretical values calculated from Equation (3) in the main text, found from $L_p = 1/\text{Im}(q)$ and $\lambda_p = 2\pi/q$, respectively. All experimental, simulated and analytical values are in excellent agreement.

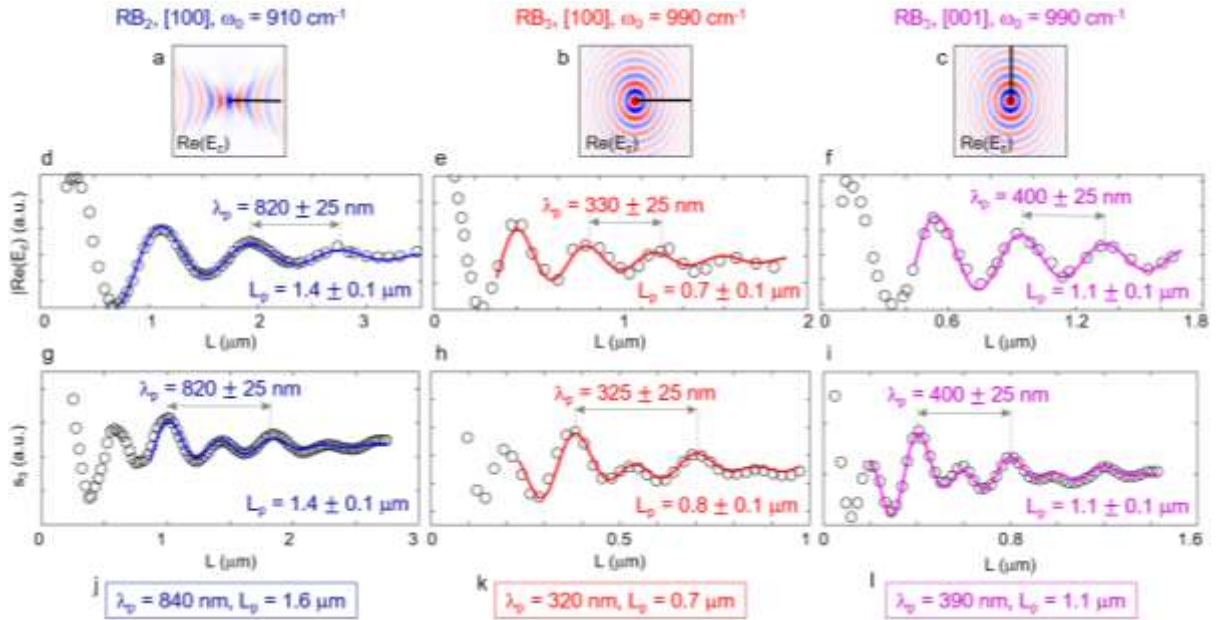


Figure S8. **a, b, c.** Field distribution of propagating PhPs launched by a point dipole oriented perpendicular to a 120-nm-thick α -MoO₃ layer for incident frequencies $\omega_0 = 910 \text{ cm}^{-1}$ (in RB₂, left column) and $\omega_0 = 990 \text{ cm}^{-1}$ (in RB₃, middle and right columns). **d, e, f.** Profiles extracted along the lines depicted in **a, b, c** (dots). By performing a fitting to Equation (S3) with $A = 0$ and $a = 1/2$, (color lines), we find the PhP propagation lengths to be $L_p = 1.4 \pm 0.1 \text{ } \mu\text{m}$ (along [100] in RB₂), $L_p = 0.7 \pm 0.1 \text{ } \mu\text{m}$ (along [100] in RB₃) and $L_p = 1.1 \pm 0.1 \text{ } \mu\text{m}$ (along [001] in RB₃). All simulations were performed using our dielectric model as input. **g, h, i.** s-SNOM (amplitude) line traces (dots) along the

120-nm flake shown in Figures 4c,e of the main text. Fits to Equation (S3) setting $a \sim 1$ are shown (color lines). The obtained propagation lengths $L_p = t_0$ are $L_p = 1.4 \pm 0.1 \mu\text{m}$ (along [100] in RB_2), $L_p = 0.8 \pm 0.1 \mu\text{m}$ (along [100] in RB_3) and $L_p = 1.1 \pm 0.1 \mu\text{m}$ (along [001] in RB_3). **j, k, i.** Theoretical values found from the analytical dispersion of PhPS, Equation (3) in the main text, yielding values in exceptional agreement with simulation and experiment: $L_p = 1.6 \mu\text{m}$ (along [100] in RB_2), $L_p = 0.7 \mu\text{m}$ (along [100] in RB_3) and $L_p = 1.1 \mu\text{m}$ (along [001] in RB_3).

S8. Attenuated total reflectance spectra (ATR) of an $\alpha\text{-MoO}_3$ flake on top of BaF_2

Finally, we examine the behavior of a $\alpha\text{-MoO}_3$ crystal when probed using ATR micro-spectroscopy. This method is based on the Kretschmann-Raether configuration for launching hyperbolic polaritons^[3,4]. In brief, a high index prism allows for coupling to modes with an effective index greater than one. One of the important parameters for this experiment is field orientation —as it is sensitive to both dielectric cavity resonances under s polarized light, and polariton resonances under p-polarized light. The optical anisotropy of $\alpha\text{-MoO}_3$ implies we also need to consider the azimuthal incident angle due to the in-plane anisotropy. This means we collect four spectra —s and p polarized along the two different crystal axes (as shown in **Figure S7**). Within this experiment we are able to probe the polaritons launched in x and z axes, as we are limited by the optical transmittance of the Ge prism. The polariton/dielectric resonances manifest as absorption dips in the spectrum —with those located around 810 cm^{-1} related to the [100] phonon, and those around 1000 cm^{-1} associated with the [010] phonon. The simulations generally match our measured spectra, with the main differences being the presence of additional peaks in the green curves, and improved sharpness in the measured ATR spectra. This is most likely due to misalignment of the incident infrared beam with the crystal axes in the ATR measurement, and the overestimation of damping for our bulk dielectric function (as discussed in the main text). However, the measurement speaks to the usefulness of our dielectric function for predicting the behavior of $\alpha\text{-MoO}_3$ samples.

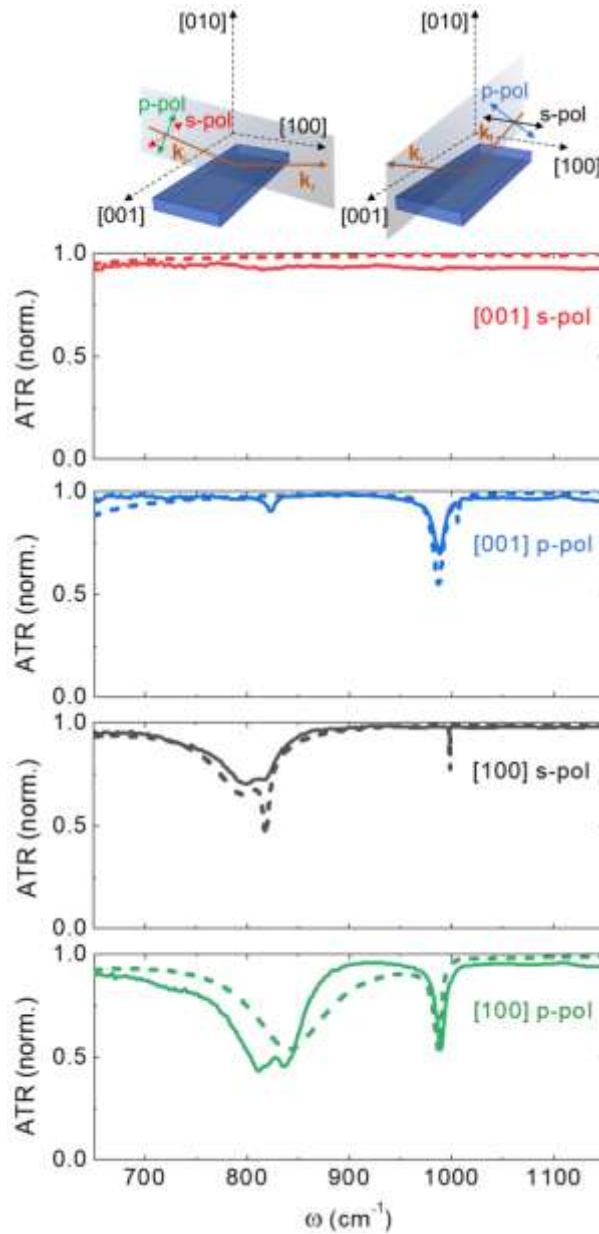


Figure S9. ATR-FTIR spectra (solid lines) on an α -MoO₃ flake (shown in Fig. 1b in the main text) along both in-plane crystal axes. Dashed lines indicate the simulated spectra, using our permittivity model as input.

S9. Comparison of our IR dielectric function parameters with prior experimental results

Table S4. Comparison of our extracted ω_{ij}^{TO} , ω_{ij}^{LO} , γ_{ij} with values reported in prior works.

Main axis	Mode index	This work		
i	j	ω_{ij}^{TO} (cm ⁻¹)	ω_{ij}^{LO} (cm ⁻¹)	γ_{ij} (cm ⁻¹)
x	1	506.7	534.3	49.1
x	2	821.4	963.0	6.0
x	3	998.7	999.2	0.35
y	1	544.6	850.1	9.5
z	1	956.7	1006.9	1.5

Main axis	Mode index	Ref. [5]			Refs. [6,7]		
i	j	ω_{ij}^{TO} (cm ⁻¹)	ω_{ij}^{LO} (cm ⁻¹)	γ_{ij} (cm ⁻¹)	ω_{ij}^{TO} (cm ⁻¹)	ω_{ij}^{LO} (cm ⁻¹)	γ_{ij} (cm ⁻¹)
x	1	-	-	-	-	-	-
x	2	820	972	4	818	974	-
x	3	-	-	-	-	-	-
y	1	545	851	4	545	851	-
z	1	958	1004	2	962	1010	-

“-”: not measured.

Table S5. Comparison of our extracted ϵ_i^∞ with values reported in prior works.

Main axis	ϵ_i^∞		
i	This work	Ref. [5]	Refs. [6,7]
x	5.78	4.0	-
y	6.07	5.2	-
z	4.47	2.4	-

“-”: not measured.

S10. Permittivity of α -MoO₃ from first principles

The dielectric function of α -MoO₃ is calculated fully *ab-initio* by making use of density functional theory (DFT) within the Perdew, Burke, and Ernzerhof parametrization of the exchange-correlation functional.^[8] Ultra-soft pseudopotentials are employed in the calculations including 6 valence electrons for O and 14 valence electrons for Mo.

The dielectric tensor, which becomes diagonal in an orthorhombic crystal, is calculated within perturbation theory.^[9] In this framework, the dielectric tensor for Cartesian directions α and β is given by

$$\epsilon_{\alpha\beta}(\omega) = \epsilon_{\alpha\beta}^\infty + 4\pi\chi_{\alpha\beta}(\omega), \quad (\text{S4})$$

where $\epsilon_{\alpha\beta}^\infty$ is the electronic contribution to the dielectric tensor (the high-frequency limit) and $\chi_{\alpha\beta}(\omega)$ is the susceptibility. The latter is expressed in atomic units as

$$\chi_{\alpha\beta}(\omega) = -\frac{1}{\Omega} \sum_i \frac{2\omega_i M_i^\alpha M_i^\beta}{\omega^2 - \omega_i^2 - 2\omega_i \Pi_i(\omega_i)}, \quad (\text{S5})$$

where Ω is the unit cell volume, ω_i the phonon frequency of the i -th mode (the sum over i is restricted to phonon modes at the Γ point), $\Pi_i(\omega_i)$ the i -th phonon mode's self-energy due to phonon-phonon interaction taken at the phonon frequency, and M_i^α is the contribution of the i -th mode to the dipole moment:

$$M_i^\alpha = \sum_{\beta s} \frac{Z_s^{\alpha\beta} e_{is}^\beta}{\sqrt{2M_s\omega_i}}. \quad (\text{S6})$$

In **Equation (S6)**, $Z_s^{\alpha\beta}$ is the effective-charge tensor for atom s , M_s the mass of atom s , and e_{is}^β the polarization vector of mode i for atom s along the Cartesian direction β .

Phonon frequencies, polarization vectors, effective charges, and the high-frequency limit of the dielectric function are calculated making use of density functional perturbation theory (DFPT)^[10] as implemented in Quantum Espresso.^[11,12] An 80 Ry energy cutoff was used for the plane-wave basis and a 800 Ry cutoff for the density. Electronic integrations were performed on an 8 x 2 x 8 grid. The phonon self-energy was calculated just including the so-called bubble contribution.^[13,14]

$$\begin{aligned} \Pi_i(\omega) = & -\frac{1}{2N_q} \sum_{qjk} |\Phi_{ijk}(0, \mathbf{q}, -\mathbf{q})|^2 \left[\frac{2(\omega_{jq} + \omega_{k-q})[1 + n_B(\omega_{jq}) + n_B(\omega_{k-q})]}{(\omega_{jq} + \omega_{k-q})^2 - (\omega + i\delta)^2} + \frac{2(\omega_{jq} - \omega_{k-q})[n_B(\omega_{k-q}) - n_B(\omega_{jq})]}{(\omega_{k-q} - \omega_{jq})^2 - (\omega + i\delta)^2} \right], \end{aligned} \quad (\text{S7})$$

In **Equation (S7)** ω_{jq} represents the j -th mode at the \mathbf{q} point of the Brillouin zone, N_q the number of \mathbf{q} points in the sum, $n_B(\omega)$ is the Bose-Einstein occupation factor, δ is a small number (10 cm⁻¹ in our case), and $\Phi_{ijk}(0, \mathbf{q}, -\mathbf{q})$ are the anharmonic third-order force constants transformed to the phonon mode basis.^[14] The third-order anharmonic force-constants are calculated by finite-differences calculating atomic forces on displaced supercells created by the ShengBTE code.^[15,16] The third-order force constants are calculated in a 2 x 1 x 2 supercell including interaction terms up to 5 nearest-neighbors. The self-energy is then calculated at 300 K by including in the sum over the \mathbf{q} points a 16 x 4 x 16 phonon grid. The

phonon frequencies and third-order force constants in this grid are obtained by Fourier interpolation. The dynamical matrices are calculated originally in a $6 \times 2 \times 6$ \mathbf{q} point grid. The *ab-initio* damping factors of the phonon mode ω_i reported in the main text correspond to the imaginary part of the phonon self-energy taken at the phonon frequency:

$$\gamma_i = -\text{Im}\Pi_i(\omega_i). \quad (\text{S8})$$

S11. THz/far-IR transmission spectra collected from α -MoO₃ powder using a Nb-superconducting bolometer

Whilst the small size of α -MoO₃ crystals precludes measurements in the far-IR, we can instead disperse a bulk powder across the surface of a THz/far-IR transparent material. Whilst this provides an ensemble averaged response of the powder, losing sensitivity to crystal axis, it does provide us with a rough estimate of the phonon energies, given by where the transmission/reflection is reduced/enhanced respectively. To perform these measurements, we dispersed α -MoO₃ crystals in IPA, via sonication for 30 min, and then drop cast on a piece of high density poly-ethylene (HDPE). We measure unpolarized reflection and transmission measurements at 40 degrees angle of incidence, shown in **Figure S8**. In general, the HDPE is weakly reflecting and moderately transmissive in the mid to far-IR. The powder sample generally shows reduced transmission and reflection—which is a consequence of scattering introduced by the crystals which have a size on the scale of the wavelength. However, at specific frequencies we observe a correlated dip in the transmission, and a peak in reflection. This suggests the presence of phonon modes at or close to these frequencies—notably 300, 349, 361 and 371 cm⁻¹. Whilst we cannot conclusively say that these correlated peaks and dips correspond to the exact phonon frequencies, this suggests that this frequency range could be of interest for future work.

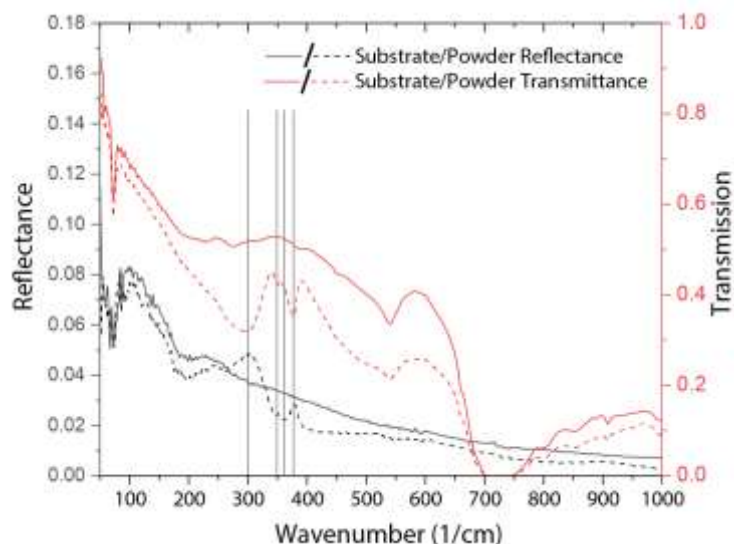


Figure S10. α - MoO_3 response in FIR/THz using reflection and transmission spectroscopy. Lines indicate correlated peaks/troughs (300 , 349 , 361 and 371 cm^{-1}), which will be associated with phonon modes.

References

- [1] A. Woessner, M. B. Lundberg, Y. Gao, A. Principi, P. Alonso-González, M. Carrega, K. Watanabe, T. Taniguchi, G. Vignale, M. Polini, J. Hone, R. Hillenbrand, F. H. L. Koppens, *Nat. Mat.*, **2015**, *14*, 421.
- [2] W. Ma, P. Alonso-González, S. Li, A. Y. Nikitin, J. Yuan, J. Martín-Sánchez, J. Taboada-Gutiérrez, I. Amenabar, P. Li, S. Vélez, C. Tollan, Z. Dai, Y. Zhang, S. Sriram, K. Kalantar-Zadeh, S.-T. Lee, R. Hillenbrand, Q. Bao, *Nature*, **2018**, *562*, 557.
- [3] T. G. Folland, L. Nordin, D. Wasserman, J. D. Caldwell, *J. Appl. Phys.*, **2019**, *125*, 191102.
- [4] T. G. Folland, T. W. W. Maß, J. R. Matson, J. R. Nolen, S. Liu, K. Watanabe, T. Taniguchi, J. H. Edgar, T. Taubner, J. D. Caldwell, *MRS Commun.*, **2018**, *8*, 1418.
- [5] Z. Zheng, N. Xu, S. L. Oscurato, M. Tamagnone, F. Sun, Y. Jiang, Y. Ke, J. Chen, W. Huang, W. L. Wilson, A. Ambrosio, S. Deng, H. Chen, *Sci. Adv.* **2019**, *5*.
- [6] K. Eda, *J. Solid State Chem.*, **1991**, *95*, 64.
- [7] M. A. Py, P. E. Schmid, J. T. Vallin, *Il Nuovo Cimento B*, **1977**, *38*, 271.
- [8] J. P. Perdew, K. Burke, M. Ernzerhof, *Phys. Rev. Lett.*, **1997**, *77*, 3865.

- [9] R. A. Cowley. *Adv. Phys.*, **1963**, *12*, 421.
- [10] S. Baroni, S. de Gironcoli, A. Dal Corso, P. Giannozzi. *Rev. Mod. Phys.*, **2001**, *73*, 515.
- [11] P. Giannozzi, S. Baroni, N. Bonini, M. Calandra, R. Car, C. Cavazzoni, D. Ceresoli, G. L. Chiarotti, M. Cococcioni, I. Dabo, A. Dal Corso, S. de Gironcoli, S. Fabris, G. Fratesi, R. Gebauer, U. Gerstmann, C. Gougoussis, A. Kokalj, M. Lazzeri, L. Martin-Samos, N. Marzari, F. Mauri, R. Mazzarello, S. Paolini, A. Pasquarello, L. Paulatto, C. Sbraccia, S. Scandolo, G. Sclauzero, A. P. Seitsonen, A. Smogunov, P. Umari, R. M. Wentzcovitch, *J. Phys. Condens. Matter.*, **2009**, *21*, 395502.
- [12] P. Giannozzi, O. Andreussi, T. Brumme, O. Bunau, M. Buongiorno Nardelli, M. Calandra, R. Car, C. Cavazzoni, D. Ceresoli, M. Cococcioni, N. Colonna, I. Carnimeo, A. Dal Corso, S. de Gironcoli, P. Delugas, R. A. DiStasio Jr, A. Ferretti, A. Floris, G. Fratesi, G. Fugallo, R. Gebauer, U. Gerstmann, F. Giustino, T. Gorni, J. Jia, M. Kawamura, H.-Y. Ko, A. Kokalj, E. Küçükbenli, M. Lazzeri, M. Marsili, N. Marzari, F. Mauri, N. L. Nguyen, H.-V. Nguyen, A. Otero-de-la-Roza, L. Paulatto, S. Poncé, D. Rocca, R. Sabatini, B. Santra, M. Schlipf, A. P. Seitsonen, A. Smogunov, I. Timrov, T. Thonhauser, P. Umari, N. Vast, X. Wu, S. Baroni, *J. Phys. Condens. Matter.*, **2017**, *29*, 465901.
- [13] L. Paulatto, F. Mauri, M. Lazzeri, *Phys. Rev. B*, **2013**, *87*, 214303.
- [14] L. Paulatto, I. Errea, M. Calandra, F. Mauri, *Phys. Rev. B*, **2015**, *91*, 054304.
- [15] W. Li, J. Carrete, N. A. Katcho, N. Mingo, *Comp. Phys. Commun.*, **2014**, *185*, 1747.
- [16] W. Li, L. Lindsay, D. A. Broido, D. A. Stewart, N. Mingo, *Phys. Rev. B*, **2012**, *86*, 174307.